catalysts

MDPI

Article

Kinetics of CO Oxidation over Unloaded and Pd-Loaded α-Fe_2O_3 Spherical Submicron Powder Catalysts: Photoacoustic Investigations at Low Pressure

Joong-Seok Roh [1], Ji-Yeong Kim [2], Joong-Gill Choi [1,*] and Sung-Han Lee [2,*]

1 Department of Chemistry, Yonsei University, Seoul 03722, Korea; rohswordsman90@hanmail.net
2 Department of Chemistry, Yonsei University, Wonju 26493, Korea; wldude9@naver.com
* Correspondence: jgchoi@yonsei.ac.kr (J.-G.C.); shl2238@yonsei.ac.kr (S.-H.L.); Tel.: +82-2-2123-2642 (J.-G.C.); +82-33-760-2238 (S.-H.L.)

Received: 29 January 2018; Accepted: 24 February 2018; Published: 28 February 2018

Abstract: In this study, α-Fe_2O_3 spherical particles with an average diameter of approximately 200 nm were synthesized by a solvothermal method for use as both a catalyst and medium for a Pd catalyst. The kinetics of CO oxidation over powders of α-Fe_2O_3 spherical particles and 14 wt % Pd/α-Fe_2O_3 spherical particles were measured in a static reactor by using a CO_2 laser-based photoacoustic technique. The total pressure was fixed at 40 Torr for the $CO/O_2/N_2$ mixture for temperatures in the range of 225–350 °C. The variation in the CO_2 photoacoustic signal with the CO_2 concentration during CO oxidation was recorded as a function of time, and the CO_2 photoacoustic data at the early reaction stage was used to estimate the rates of CO_2 formation. Based on plots of ln(rate) vs. $1/T$, apparent activation energies were calculated as 13.4 kcal/mol for the α-Fe_2O_3 submicron powder and 13.2 kcal/mol for the 14 wt % Pd/α-Fe_2O_3 submicron powder. Reaction orders with respect to CO and O_2 were determined from the rates measured at various partial pressures of CO and O_2 at 350 °C. The zero-order of the reaction with respect to Po_2 was observed for CO oxidation over α-Fe_2O_3 submicron powder, while 0.48 order to Po_2 was observed for CO oxidation over Pd/α-Fe_2O_3 submicron powder. The partial orders with respect to P_{CO} were determined as 0.58 and 0.54 for the α-Fe_2O_3, and the Pd/α-Fe_2O_3 submicron powders, respectively. The kinetic results obtained from both catalysts were compared with those for the α-Fe_2O_3 fine powder catalysts and were used to understand the reaction mechanism.

Keywords: photoacoustic technique; kinetics of CO oxidation; α-Fe_2O_3 spherical powder catalyst; Pd/α-Fe_2O_3 catalyst

1. Introduction

It is widely known that CO oxidation is one of the most important reactions in environmental research. Extant studies [1] indicate that transition metal oxides, including MnO_2, Fe_2O_3, Co_2O_3, NiO, and CuO, as well as noble metals, are highly active for CO oxidation. The catalytic performance of metal oxides is enhanced by increasing their surface area. Thus, metal oxide catalysts were synthesized in the forms of nanoparticles to yield high surface areas. Generally, nanostructured metal oxides are significantly active catalysts when compared with non-nanostructured metal oxides. However, it is not easy to utilize these oxides as a medium for noble metal catalysts due to their extremely small size. Among the transition metal oxides, iron oxide is synthesized in the form of spherical particles with a controlled size, which attracts research attention with respect to its utilization as support. Noble metals on Fe_2O_3 particles were indicated as appreciably active [2]. Recently, Fe_2O_3 was frequently used as a model system in studies that focused on strong metal–support interactions [3]. Specifically,

Fe_2O_3 spherical particles with a submicron size have been rarely examined as a catalyst and support to date.

In any kinetics study, monitoring the time-dependent variation of the concentrations of reactants and/or products is considered to be crucial. It has been known that photoacoustic spectroscopy (PAS) is suitable to in situ monitor a reaction processes in its initial stage [4]. Since signals obtained from PAS rely on the concentration of a target species and PAS detects extremely low level molecular gases with high selectivity and large signal intensity, temporal variations in concentration can be readily measured even in a short period of reaction times where rates are high. Thus, low molecular level photoacoustic results are believed to provide more accurate kinetic information for catalytic reactions, especially when the reaction occurs on a relatively clean surface of catalysis.

In this study, we prepared α-Fe_2O_3 spherical particles (sp) with an average diameter of approximately 200 nm by using a solvothermal method. Subsequently, α-Fe_2O_3 submicron powder was tested as a catalyst for CO oxidation and as a medium for a Pd metal catalyst. CO oxidation from α-Fe_2O_3 and Pd/α-Fe_2O_3 submicron powder catalysts was performed in a static reactor at a total pressure of 40 Torr. A CO_2, laser-based, photoacoustic technique with a differential photoacoustic cell was employed to investigate the kinetics of CO oxidation. Rates of CO_2 formation were calculated from the CO_2 photoacoustic data at an early reaction stage. The rates were measured with a stoichiometric reaction mixture and aided in determining the apparent activation energies in the temperature range of 225–350 °C. The partial orders with respect to CO and O_2 were calculated from the rates that were measured at various partial pressures of CO and O_2 at 350 °C. The catalytic behaviors of both the α-Fe_2O_3 and Pd/α-Fe_2O_3 submicron powders for CO oxidation were compared with those of an α-Fe_2O_3 fine powder.

2. Results

Figure 1A shows the X-ray powder diffraction (XRD) pattern of magnetite spherical submicron particles that were directly prepared by using a solvothermal method. The diffraction pattern indicates that the magnetite phase has a face-centered cubic structure (JCPDS Card No. 00-039-1346). The magnetite powder was calcined at 600 °C in a flow of O_2 (10%)/He mixture, and a red powder was obtained. Figure 1B shows the XRD pattern of the red powder and indicates that the red powder corresponds to an α-Fe_2O_3 phase with a rhombohedral structure (JCPDS Card No. 01-089-0598). In this study, Pd-loaded α-Fe_2O_3 spherical submicron particles were prepared by using the impregnation method. Figure 1C shows the XRD pattern of the Pd/α-Fe_2O_3 particles, which exhibits reflection peaks arising from Pd metal crystallites with a face-centered cubic structure (JCPDS Card No. 87-0641) at 2θ = 40.1°, 46.6°, and 68.1° as denoted by the Miller indices (111), (200), and (220), respectively. By performing energy dispersive X-ray spectroscopy (EDS) on the Pd/α-Fe_2O_3 sample, the Pd/Fe atomic ratio was determined as 0.123, which corresponds to 14 wt % Pd.

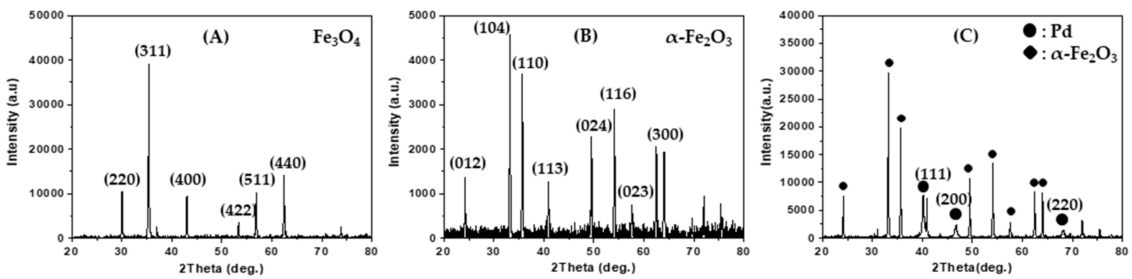

Figure 1. XRD patterns of (**A**) as-prepared Fe_3O_4 powder, (**B**) calcined Fe_3O_4 (α-Fe_2O_3 (sp200)), and (**C**) Pd/α-Fe_2O_3 (sp200). Fe_3O_4 (JCPDS No. 00-039-1346); α-Fe_2O_3 (JCPDS No. 01-089-0958); Pd (JCPDS No. 7440-05-3).

Figure 2A shows a field emission-scanning electron microscopy (FE-SEM) image of the α-Fe_2O_3 spherical submicron particles and indicates that the particles possess a spherical morphology with a rough surface. Figure 2B exhibits a high-resolution transmission electron microscopy (HR-TEM) image of the α-Fe_2O_3 spherical submicron particles. Figure 2C displays a FE-SEM image of the Pd (14 wt %)-loaded α-Fe_2O_3 spherical submicron particles and shows that Pd nano-particles are loaded on the surface of α-Fe_2O_3 spherical submicron particles.

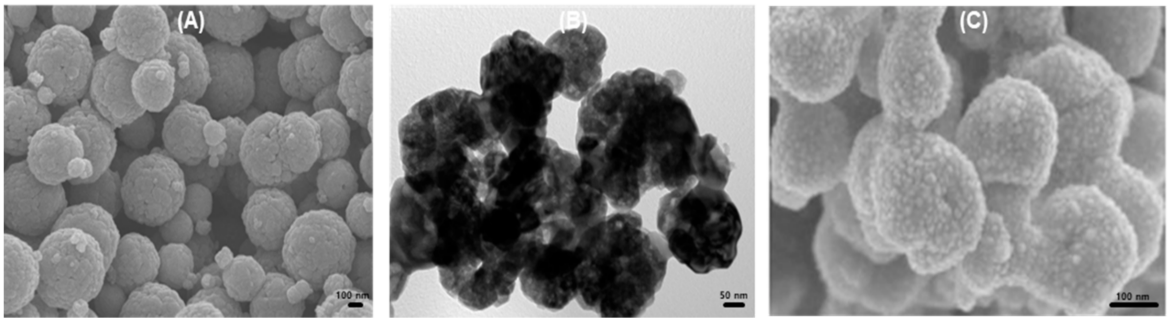

Figure 2. (**A**) SEM image of magnetite (sp200) powder, (**B**) TEM image of α-Fe_2O_3 (sp200) powder, and (**C**) SEM image of Pd (14 wt %)/α-Fe_2O_3 (sp200) powder.

Figure 3A shows the particle size distribution of the α-Fe_2O_3 spherical submicron particles. From the histogram, the mean diameter of the α-Fe_2O_3 spherical submicron particles was estimated to be 196 nm. The α-Fe_2O_3 spherical submicron powder sample is denoted as α-Fe_2O_3 (sp200). N_2 adsorption measurements were performed for the α-Fe_2O_3 (sp200) sample at liquid nitrogen temperature. The N_2 adsorption–desorption isotherm is shown in Figure 3B. An International Union of Pure and Applied Chemistry (IUPAC) classification reveals that the hysteresis loop of Figure 3B corresponds to the H3 type [5]. Figure 3C reveals the pore size distribution as determined by the Barret–Joyer–Halenda (BJH) method from the adsorption branch of the isotherm and shows that the pore size is distributed in the range of 3–20 nm. The Brunauer–Emmett–Teller (BET) surface area was calculated to be 19.0 m^2/g for the α-Fe_2O_3 (sp200) powder, 7.4 m^2/g for the Pd/α-Fe_2O_3 (sp200) powder, and 6.8 m^2/g for the α-Fe_2O_3 fine powder (α-Fe_2O_3 (fp)). The surface area of the Pd/α-Fe_2O_3 (sp200) is smaller than that of α-Fe_2O_3 (sp200), suggesting that the openings of some pores could be blocked by the Pd particles.

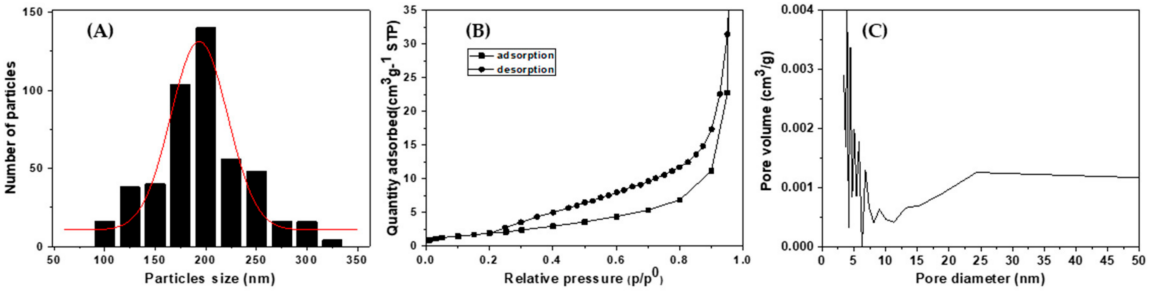

Figure 3. (**A**) Particle size distribution, (**B**) N_2 adsorption–desorption isotherm, and (**C**) pore size distribution of α-Fe_2O_3 (sp200) powder.

A kinetic study of CO oxidation was performed with the static method, and photoacoustic spectroscopy was employed to measure the rate of CO_2 formation in the early reaction stage of CO oxidation. Generally, the CO_2 photoacoustic signal measured with the CO_2 laser-based photoacoustic method is dependent on the excitation wavelength, the power of the light source, the chopping frequency, and the sensitivity of the microphone. Figure 4A shows that the CO_2 photoacoustic signal

as a function of laser power exhibits an optimal linearity in the range from 1–4 W. Figure 4B displays the CO_2 photoacoustic signal measured as a function of CO_2 partial pressure and indicates that the signal is linear for CO_2 partial pressures below 12 Torr. Accordingly, subsequent measurements were performed with a CO_2 partial pressure below 12 Torr and a CO_2 laser power of 3 W. A blank test was performed by using a $CO/O_2/N_2$ (20/10/10 Torr) mixture in the temperature range of 25–400 °C, which revealed that variations in the CO_2 photoacoustic signal were absent. The effect of temperature on the rate of CO_2 formation for the catalytic reaction in the static reactor was investigated by using a $CO/O_2/N_2$ (20/10/10 Torr) mixture in the temperature range of 175–350 °C.

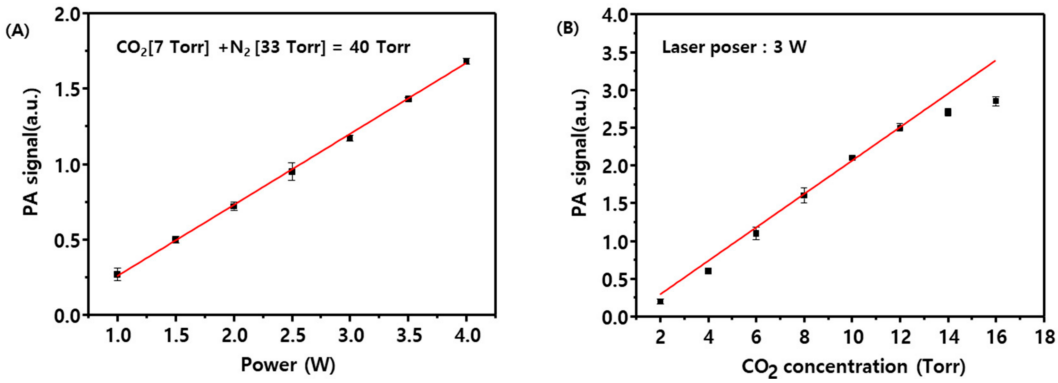

Figure 4. Variations of CO_2 photoacoustic (PA) signals with (**A**) laser input power and (**B**) CO_2 concentration.

Figure 5 shows variations in the CO_2 photoacoustic signal relative to time for CO oxidation over catalysts at various temperatures. The rates of CO_2 formation were calculated from the CO_2 photoacoustic signals obtained in the reaction period range of 60–180 s after the injection of the reaction mixture into the static reactor.

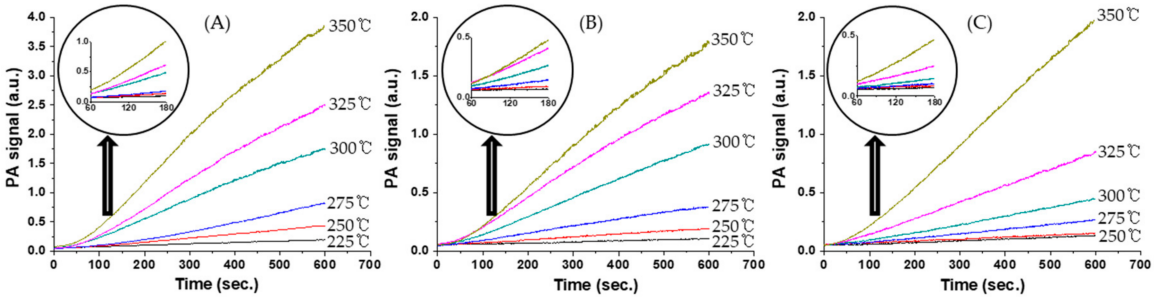

Figure 5. Variations of CO_2 photoacoustic signals with time for CO oxidation over (**A**) α-Fe_2O_3 fine powder (fp) (**B**) α-Fe_2O_3 (sp200) powder, and (**C**) 14 wt % Pd/α-Fe_2O_3 (sp200) powder at various temperatures.

The rates were plotted as a function of reciprocal temperature according to the Arrhenius-type equation given by rate ∞ $\exp(-E_a/RT)$ as shown in Figure 6. From the slopes of the linear curves in the temperature range of 225–350 °C, apparent activation energies were calculated as 16.8 ($\pm$0.3) kcal/mol for the α-Fe_2O_3 (fp), 13.4 ($\pm$0.1) kcal/mol for the α-Fe_2O_3 (sp200), and 13.2 ($\pm$0.5) kcal/mol for the Pd/α-Fe_2O_3 (sp200). Reaction orders with respect to P_{CO} and Po_2 were determined from the rates measured at various partial pressures of CO and O_2 at 350 °C. The rates were plotted as a function of partial pressures of CO and O_2 which based on the power rate law should follow rate $= k(Pco)^m(Po_2)^n$.

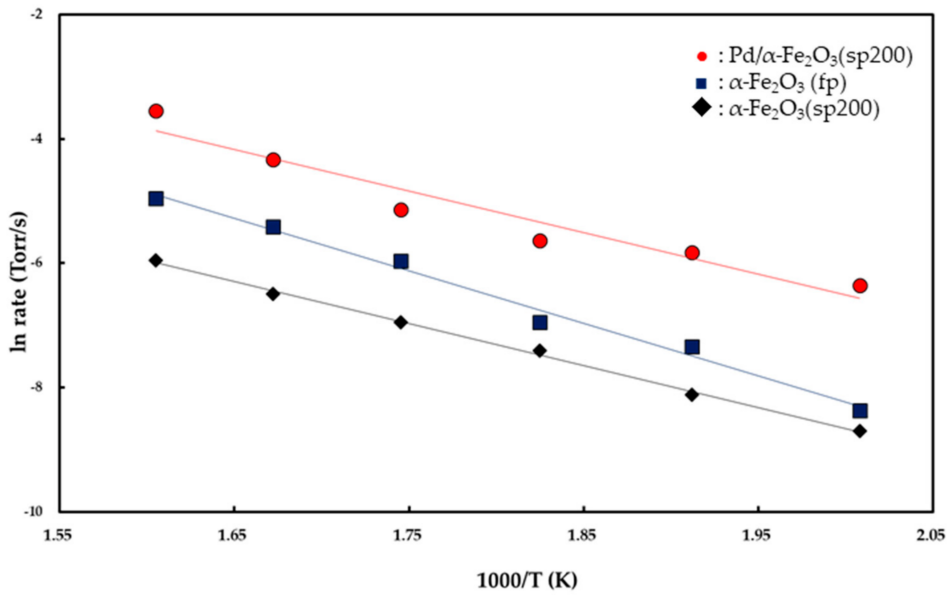

Figure 6. Arrhenius plots for CO oxidation over α-Fe_2O_3 (fp), α-Fe_2O_3 (fp200), and 14 wt % Pd/α-Fe_2O_3 (sp200) catalysts in the temperature range of 225–350 °C.

Figures 7 and 8 show the *P*co and Po_2 dependencies of the rate of CO_2 formation, respectively. Partial orders with respect to *P*co and Po_2 were determined from the slopes of the linear curves. Both the α-Fe_2O_3 (fp) and α-Fe_2O_3 (sp200) catalysts exhibited zero-order kinetics for Po_2 while the Pd/α-Fe_2O_3 (sp200) catalyst showed 0.48 (±0.03)-order with respect to Po_2. The partial order with respect to P_{CO} was determined to be 0.85 (±0.03)-order for the α-Fe_2O_3 (fp) catalyst, 0.58 (±0.1)-order for the α-Fe_2O_3 (sp200) catalyst, and 0.54 (±0.06)-order for the Pd/α-Fe_2O_3 (sp200) catalyst.

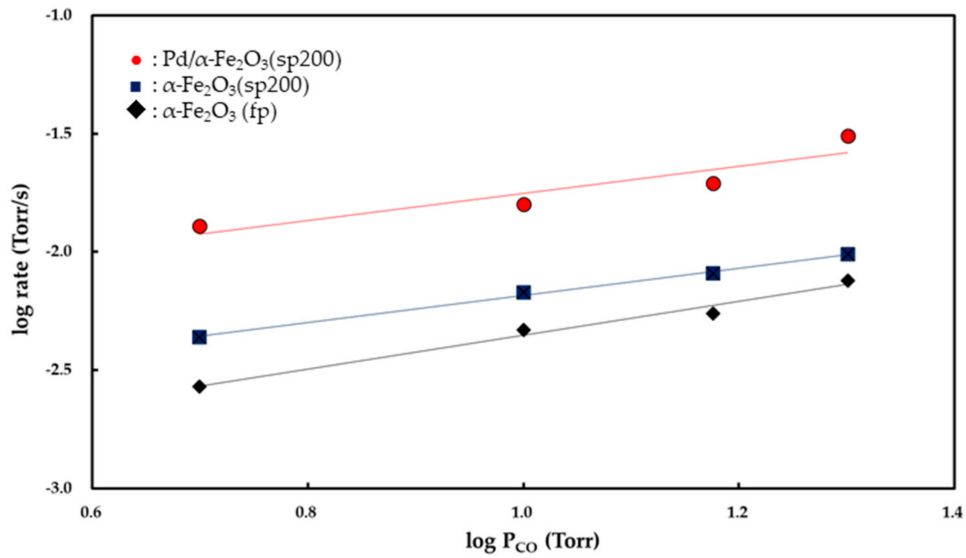

Figure 7. *P*co dependencies of rates for CO oxidation over α-Fe_2O_3 (fp), α-Fe_2O_3 (sp200), and 14 wt % Pd/α-Fe_2O_3 (sp200) catalysts at 350 °C.

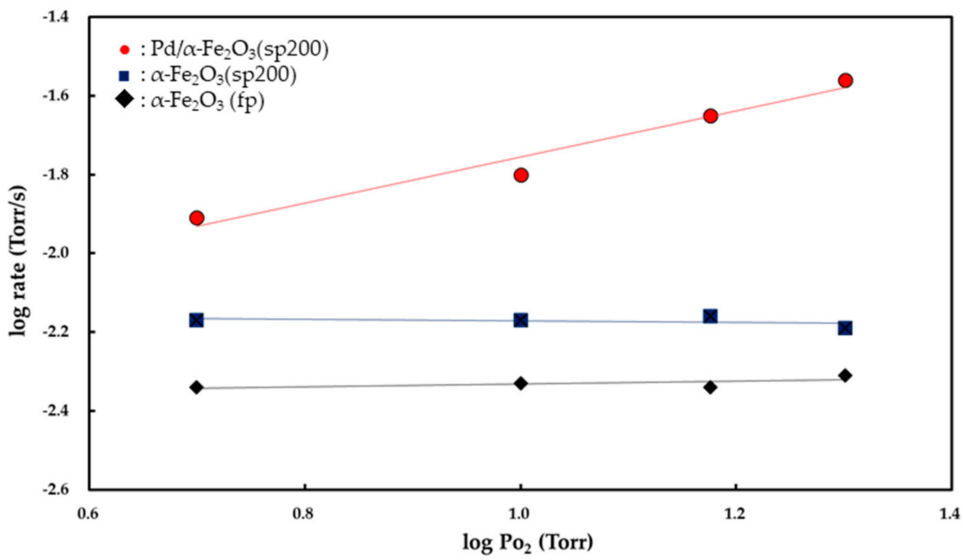

Figure 8. Po_2 dependencies of rates for CO oxidation over α-Fe_2O_3 (fp), α-Fe_2O_3 (sp200), and 14 wt % Pd/α-Fe_2O_3 (sp200) catalysts at 350 °C.

3. Discussion

With respect to CO oxidation over Fe_2O_3, it was reported that Fe_2O_3 acts as a catalyst in the presence of O_2 (g) and as a direct oxidant for CO (g) in the absence of O_2 (g) [6,7]. In the presence of O_2, the Fe_2O_3 surface is primarily reduced by CO (g), and the reduced Fe_2O_3 surface is successively re-oxidized by O_2 (g). In the catalytic oxidation of CO, the CO disproportion reaction (the Boudourd reaction corresponding to 2CO (g)$\rightleftarrows$ (s) + CO_2 (g)) is considered as a side reaction because it is thermodynamically feasible below 630 °C based on the assumption of the standard free energy change $\Delta G^0 = 0$. According to Li et al. [6], with respect to CO oxidation on Fe_2O_3 nanopowder, the CO disproportion reaction occurs above 300 °C in the absence of O_2 (g). The photoacoustic measurements in our work were performed by using a CO/O_2 mixture at a total pressure of 40 Torr, and accordingly, the occurrence of CO disproportion is considered as infeasible under the reaction conditions.

As shown in Figure 6, the apparent activation energies for CO oxidation were determined as 16.8 (±0.3) kcal/mol for the Fe_2O_3 (fp) catalyst and 13.4 (±0.1) kcal/mol for the Fe_2O_3 (sp200) catalyst in the temperature range of 225–350 °C. It is expected from the magnitude of the apparent activation energies that the reactants are chemisorbed on the catalyst surface. Specifically, Fe_2O_3 is oxygen deficient and oxygen vacancies are considered as the predominant defect for the oxide. Oxygen vacancies are readily generated in the oxide when Fe_2O_3 is heated at a low pressure [8,9]. Typically, oxygen vacancies in metal oxides act as adsorption sites for O_2 (g) because they serve as electron donors. When O_2 (g) is adsorbed (ads) on the oxygen vacancy, it is dissociated into two oxygen atoms as follows:

$$O_2\ (g) + 2e^- \rightleftarrows 2O^-\ (ads) \quad (1)$$

$$O^-\ (ads) + e^- \rightleftarrows O^{2-}\ (latt) \quad (2)$$

where e^- represents an electron trapped at the oxygen vacancy site. Given that an O^- (ads) ion is active, CO (g) reacts with O^- (ads) to form $CO_2{}^-$ (ads): CO (g) + O^- (ads) $\rightleftarrows$ $CO_2{}^-$ (ads). The resultant $CO_2{}^-$ (ads) ion is desorbed from the surface to produce CO_2 (g) and the oxygen vacancy is simultaneously regenerated in the oxide.

If the O^- (ads) ions act as adsorption sites for CO (g) to form CO_2 (g), then the partial order with respect to O_2 is derived to be 0.5 [4]. In this study, as shown in Figure 8, the rates of CO_2 formation for both the Fe_2O_3 (fp) and Fe_2O_3 (sp200) powders were obtained as independent of Po_2, and this

indicates that the surface is continuously saturated by O_2 (g). The zero-order kinetics for Po_2 suggests that CO (g) preferably reacts with O^{2-} (latt) as opposed to the O^- (ads) ion. The interaction between CO (g) and the lattice (latt) oxygen of Fe_2O_3 is described by the following equilibrium:

$$CO\ (g) + O^{2-}\ (latt) \rightleftarrows CO_2{}^-(ads) + e^- \quad (3)$$

When the $CO_2{}^-$ (ads) ion reacts further with O^{2-} (latt), a carbonate ion is formed as follows:

$$CO_2{}^-\ (ads) + O^{2-}\ (latt) \rightleftarrows CO_3{}^{2-}\ (ads) + e^- \quad (4)$$

The carbonate ion is decomposed into CO_2 (g) according to the following reaction: $CO_3{}^{2-}$ (ads) $\rightarrow CO_2$ (g) + O^{2-} (latt). If Equations (3) and (4) are included in the reaction mechanism, then the rate law is derived as first-order kinetics for *P*co based on the assumption of constant [O^{2-} (latt)] [4]. In this study, the partial order to *P*co is determined as 0.85 (±0.03)-order for the α-Fe_2O_3 (fp) catalyst and 0.58 (±0.1)-order for the α-Fe_2O_3 (sp200) catalyst, thereby suggesting that an inhibition process by CO_2 is included in the reaction mechanism under the reaction conditions.

Previous studies of CO_2 adsorption on Fe_2O_3 [10,11] indicate that CO_2 is chemisorbed on the surface of iron oxide to form bidentate carbonate. Several studies suggested that oxygen vacancies in metal oxide act as adsorption sites for CO_2 as well as O_2, wherein CO_2 (g) is chemisorbed on oxygen vacancies and the resultant CO_2 (ads) further reacts with O^{2-} (latt) to form carbonate ions [12–17]. Oxygen vacancies are considered as predominant defects in Fe_2O_3, and thus it is feasible to form a carbonate species on the surface of Fe_2O_3. If CO_2 is adsorbed on the lattice oxygen of Fe_2O_3, then CO_2 (g) is in equilibrium with carbonate ions according to the following equilibrium: CO_2 (g) + O^{2-} (latt) $\rightleftarrows CO_3{}^{2-}$ (ads). When both CO and CO_2 competitively interact with the lattice oxygen, the partial order with respect to *P*co is observed as a value less than 1. As shown in Figure 7, the partial order to *P*co for CO oxidation over Fe_2O_3 (sp200) was observed as 0.54 (±0.06), and this value is lower than 0.85 (±0.03) for the reaction relative to Fe_2O_3 (fp). These results suggest that the inhibition process by CO_2 is more feasible on Fe_2O_3 (sp200) as opposed to the Fe_2O_3 (fp).

Conversely, the apparent activation energy for CO oxidation on the Pd/Fe_2O_3 (sp200) catalyst is 13.2 kcal/mol, as shown in Figure 6. This value is in good agreement with 13.3 kcal/mol for CO oxidation on 1 wt % Pd/FeO_x in the temperature range of 120–160 °C [2] and 12.5 kcal/mol on 5 wt % Pd/Al_2O_3 in the temperature range of 120–160 °C [18], although it slightly exceeds 8.2 kcal/mol on 1.9 wt % Pd/FeO_x in the temperature range of 5–80 °C [19]. As shown in Figure 8, the partial order with respect to Po_2 on the Pd/Fe_2O_3 (sp200) catalyst is 0.48 (±0.03)-order, and this is entirely different from the zero-order kinetics observed for both the Fe_2O_3 (sp200) and Fe_2O_3 (fp) catalysts. The 0.48 (±0.03)-order is close to 0.5-order, and thus it is possible to consider that O_2 (g) is dissociatively adsorbed on the Pd surface to form two oxygen atoms (O^- (ads)) based on equilibrium (1). Therefore, CO (g) is easily adsorbed on the active O^- (ads) ion to form $CO_2{}^-$ (ads) as follows:

$$CO\ (g) + O^-\ (ads) \rightleftarrows CO_2{}^-\ (ads) \quad (5)$$

$$CO_2{}^-\ (ads) \rightarrow CO_2\ (g) + e^- \quad (6)$$

When CO (g) reacts with the O^- (ads) ion to produce CO_2 (g) based on Reactions (5) and (6), the partial order to Po_2 is derived to be 0.5-order [8]. The 0.48 (±0.03)-order obtained in this study supports that O_2 (g) is dissociatively adsorbed on the surface of Pd. The partial order to *P*co for the Pd/Fe_2O_3 (sp200) catalyst, determined to be 0.58 (±0.1), implies that the inhibition process by CO_2 is involved in the reaction mechanism. The O^- (ads) ions formed on the Pd surface act as an adsorption site for CO_2 (g). If CO_2 (g) is adsorbed on O^- (ads), then carbonate ions are formed according to the following equilibrium:

$$CO_2\ (g) + O^-\ (ads) + e^- \rightleftarrows CO_3{}^{2-}\ (ads) \quad (7)$$

This implies that CO_2 (g) inhibits CO_2 formation via the reaction between CO (g) and O^- (ads). Although it is not possible to exclude oxygen spillover from Fe_2O_3 to the Pd surface in the reaction mechanism, the kinetic results for CO oxidation over Pd/Fe_2O_3 (sp200) suggest that CO (g) favorably reacts with O^- (ads) to form $CO_2{}^-$ (ads). The $CO_2{}^-$ (ads) further reacts with O^- (ads) to produce $CO_3{}^{2-}$ (ads), and the resultant $CO_3{}^{2-}$ (ads) decomposes into CO_2 (g). When both CO (g) and CO_2 (g) are competitively adsorbed on the O^- (ads) on the Pd surface, the partial order to *P*co is observed as a value below 1 as obtained for the Pd/Fe_2O_3 (sp200) catalyst (0.58 (±0.1)-order).

4. Experimental

The α-Fe_2O_3 spherical submicron particles were synthesized from $FeCl_3 \cdot 6H_2O$ (97%, Aldrich-Sigma, St. Louis, MO, USA), sodium acetate trihydrate (NaAc) (≥99%, Sigma-Aldrich, St. Louis, MO, USA), ethylene glycol (EG) (≥99%, Sigma-Aldrich, St. Louis, MO, USA), and diethylene glycol (DEG) (≥99%, Sigma-Aldrich, St. Louis, MO, USA) by the solvothermal method [20,21]. Specifically, NaAc (1.5 g) was dissolved in a mixture of EG (20 mL) and DEG (20 mL) at 60 °C with constant stirring for 30 min. Subsequently, $FeCl_3 \cdot 6H_2O$ (1.08 g) was dissolved in the NaAc solution with vigorous stirring for 30 min. The formation of viscous slurry was transferred into a teflon-line stainless-steel autoclave with 50 mL capacity. The autoclave was maintained at 200 °C for 10 h and cooled to room temperature to obtain precipitates. The resulting precipitates were rinsed with distilled water and absolute alcohol several times, dried at 60 °C for 6 h, and a black powder was obtained. The black powder (Fe_3O_4) was calcined at 500 °C in air, cooled to room temperature, and a red powder (α-Fe_2O_3) was obtained as a final product. Furthermore, α-Fe_2O_3-supported Pd was prepared according to the following procedures: the Fe_2O_3 submicron particles were dispersed in ethanol, followed by sonication for 3 h at room temperature by using an ultrasonic cleaner, and $PdCl_2$ was added into the mixture. After sonication for 3 h, a hydrazine solution was dropped into the suspension while stirring, in which Pd^{2+} was reduced to Pd^0 by hydrazine [22,23]. The precipitates were separated by centrifugation, washed with ethanol five times, and the Pd/Fe_2O_3 sample was obtained. In this study, α-Fe_2O_3 fine powder, used as a reference material, was prepared by the wet method by using $FeCl_3$ and NH_4OH solution [24].

The phase identification of the sample was performed by using XRD and using a D/max-RB diffractometer (Rigaku, The Woodlands, TX, USA). The size, morphology, and chemical composition of the spherical particles were determined by using FE-SEM (JEOL-6701F, JEOL, Tokyo, Japan) equipped with an energy dispersive X-ray spectroscopy (EDS). In order to measure the surface area and porosity of samples, N_2 adsorption measurements were conducted with a Micromeritics Autosorb-iQ 2ST/MP instrument (Quantachrome Instruments, Boynton Beach, FL, USA).

Kinetic measurements of CO oxidation were performed in a static reactor by using a CO_2 laser-based photoacoustic technique. As indicated in a previous study [4], the photoacoustic technique with a differential photoacoustic cell was proven as a suitable technique for in situ monitoring of the change in the CO_2 concentration during the catalytic oxidation of CO. The differential photoacoustic cell was composed of a reference cell and a sample cell that were separated from each other by a ZnSe window. The reference cell was filled with a gaseous mixture of CO_2 (0.2 Torr) and N_2 (39.8 Torr), and the sample cell was directly connected to the reactor that was composed of quartz tubing with a volume of 21 cm^3. The photoacoustic cell was a Helmholtz resonator with a diameter of 19 mm and a length of 33 mm, with an adjoining tube with a diameter of 1 mm and a length of 28 mm. Additionally, CO_2 photoacoustic signals from the microphones attached to the sample (signal A) and reference (signal B) cells were detected by a lock-in amplifier (EG & G Princeton Applied Research Model 5210). The signal ratio (A/B) was recorded as a function of time by using a personal computer. The total pressure ($CO/O_2/N_2$) in the reactor was maintained at 40 Torr and filled with N_2 as a buffer gas. The purity of gases exceeded 99.999%, and the gases were dehydrated with suitable filters. The output beam of a continuous wave (cw) CO_2 laser (Synrad Series 48-1-28) operating in multilines of 10.6 μm

was modulated at the nonresonance condition of 20 Hz. The rates of CO_2 formation for the catalytic reaction were estimated from the CO_2 photoacoustic data in the early reaction stage.

5. Conclusions

CO oxidations over Fe_2O_3 (fp), Fe_2O_3 (sp200), and 14 wt % Pd/Fe_2O_3 (sp200) catalysts were kinetically measured by using a photoacoustic technique in a static reactor at a total pressure of 40 Torr. The partial order with respect to O_2 was observed as zero-order for both the Fe_2O_3 (fp) and Fe_2O_3 (sp200) catalysts and observed as 0.48-order for the 14 wt % Pd/Fe_2O_3 (sp200) catalyst. The surface of Fe_2O_3 (fp) and Fe_2O_3 (sp200) catalysts is considered as continuously saturated by O_2 (g) adsorption to form lattice oxygens. However, in the case of the Pd/Fe_2O_3 (sp200) catalyst, O_2 (g) is dissociatively adsorbed on the Pd surface to form two oxygen atoms (O^- (ads)). The kinetic results suggest that CO (g) is chemisorbed on the lattice oxygen with respect to the Fe_2O_3 (fp) and Fe_2O_3 (sp200) catalysts. Conversely, CO is preferably adsorbed on the O^- (ads) ion with respect to the Pd/Fe_2O_3 (sp200) catalyst. With respect to CO oxidation, the Fe_2O_3 (fp), Fe_2O_3 (sp200), and Pd/Fe_2O_3 (sp200) catalysts indicated that the partial orders with respect to *P*co are less than 1, which suggests that an inhibition process by CO_2 is included in the reaction mechanisms.

It is considered that the kinetic data collected at the early stages of a catalytic reaction comprising relatively high reaction rates are different from those obtained at later stages that can be controlled by constant activity of the catalyst. It is also noted that the kinetic measurement of a catalytic reaction at a high-pressure condition can be more advantageous to integrated kinetic analysis because the rate of a catalytic reaction is proportional to the surface coverage, which depends on the pressure of gaseous reactants. Nevertheless, it is noticeable that the photoacoustic signals showed a linear relationship with the concentration of species of interest even under low pressure conditions and can be recorded as a function of time-on-stream during the reaction process. Hence, PAS is suitable to study reaction kinetics at the molecular level during the early stages of catalytic oxidation of CO, providing relevant information on the reaction mechanism.

Acknowledgments: This research was partially supported by the Basic Science Research Program through the National Research Foundation of Korea (NRF) funded by the Ministry of Science, ICT and Future Planning (NRF-2012R1A1A2005806). J.-G.C. also thanks to Hyundai Electric and Energy Systems Co. for their partial support.

Author Contributions: J.-S.R. performed catalytic experiments and J.-Y.K. synthesized and characterized the catalysts. S.-H.L. and J.-G.C. managed all the experimental and writing process as the corresponding authors.

Conflicts of Interest: The authors declare no conflict of interest.

References

1. Cimino, A.; Carra, S. Chemisorption and catalysis on metal oxides. In *Electrodes of Conductive Metallic Oxides*; Trasatti, S., Ed.; Elsevier: Amsterdam, The Netherlands, 1980; pp. 97–140.
2. Jain, D.; Madras, G. Mechanistic Insights and Kinetics of CO Oxidation over Pristine and Noble Metal Modified Fe_2O_3 Using Diffuse Reflectance Infrared Fourier Transform Spectroscopy. *Ind. Eng. Chem. Res.* **2017**, *56*, 2008–2024. [CrossRef]
3. Kast, P.; Friedrich, M.; Teschner, D.; Girgsdies, F.; Lunkenbein, T.; d'Alnoncourt, R.N.; Behrens, M.; Schlögl, R. CO oxidation as a test reaction for strong metal-support interaction in nanostructured Pd/FeO_x powder catalysts. *Appl. Catal. A* **2015**, *502*, 8–17. [CrossRef]
4. Jung, H.J.; Lim, J.T.; Lee, S.H.; Kim, Y.R.; Choi, J.G. Kinetics and Mechanisms of CO Oxidation on $Nd_{1-x}Sr_xCoO_{3-y}$ Catalysts with Static and Flow Methods. *J. Phys. Chem.* **1996**, *100*, 10243–10248. [CrossRef]
5. Kaneko, K.J. Determination of pore size and pore size distribution: 1. Adsorbents and catalysts. *Membr. Sci.* **1994**, *96*, 59–89. [CrossRef]
6. Li, P.; Miser, D.E.; Rabiel, S.; Yadav, R.T.; Hajaligol, M.R. The removal of carbon monoxide by iron oxide nanoparticles. *Appl. Catal. B* **2003**, *43*, 151–162. [CrossRef]

7. Cao, J.-L.; Wang, Y.; Yu, X.-L.; Wang, S.-R.; Wu, S.-H.; Yuan, Z.-Y. Mesoporous CuO–Fe_2O_3 composite catalysts for low-temperature carbon monoxide oxidation. *Appl. Catal. B* **2008**, *79*, 26–34. [CrossRef]
8. Blank, S.L.; Pask, J.A. Diffusion of iron and nickel in magnesium oxide single crystals. *J. Am. Ceram. Soc.* **1969**, *52*, 669–675. [CrossRef]
9. Kim, K.H.; Lee, S.H.; Choi, J.S. Electrical conductivity of pure and doped α-ferric oxides. *J. Phys. Chem. Solids* **1985**, *46*, 331–338. [CrossRef]
10. Baltrusaitis, J.; Schuttlefield, J.; Zeitler, E.; Grassian, V.H. Carbon dioxide adsorption on oxide nanoparticle surfaces. *Chem. Eng. J.* **2011**, *170*, 471–481. [CrossRef]
11. Smit, G.; Strukan, N.; Craje, M.W.J.; Lazar, K. A comparative study of CO adsorption and oxidation on Au/Fe_2O_3 catalysts by FT-IR and in situ DRIFTS spectroscopies. *J. Mol. Catal. A* **2006**, *252*, 163–170. [CrossRef]
12. Otsuka, K.; Hatano, M.; Morikawa, A. Hydrogen from water by reduced cerium oxide. *J. Catal.* **1983**, *79*, 493–496. [CrossRef]
13. Wang, C.; Yin, H.; Dai, S. A general approach to noble metal− metal oxide dumbbell nanoparticles and their catalytic application for CO oxidation. *Chem. Mater.* **2010**, *22*, 3277–3282. [CrossRef]
14. Sharma, S.; Hilaire, S.; Vohs, J.M.; Grote, R.J.; Jen, H.W. Evidence for Oxidation of Ceria by CO_2. *J. Catal.* **2000**, *190*, 199–204. [CrossRef]
15. Bernal, S.; Blanco, G.; Gatica, J.M.; Larese, C.; Vidal, H. Effect of Mild Re-oxidation Treatments with CO_2 on the Chemisorption Capability of a Pt/CeO_2 Catalyst Reduced at 500 °C. *J. Catal.* **2001**, *200*, 411–415. [CrossRef]
16. Demoulin, O.; Navez, M.; Mugabo, J.L.; Ruiz, P. The oxidizing role of CO_2 at mild temperature on ceria-based catalysts. *Appl. Catal. B* **2007**, *70*, 284–293. [CrossRef]
17. Staudt, T.; Lykhach, Y.; Tsud, N.; Skála, T.; Prince, K.C.; Matolín, V.; Libuda, J. Ceria reoxidation by CO_2: A model study. *J. Catal.* **2010**, *275*, 181–185. [CrossRef]
18. Perry, W.L.; Katz, J.D.; Rees, D.; Paffet, M.T.; Datye, A.K. Kinetics of the microwave-heated CO oxidation reaction over alumina-supported Pd and Pt catalysts. *J. Catal.* **1997**, *171*, 431–438. [CrossRef]
19. Liu, L.; Zhou, F.; Wang, L.; Qi, X.; Shi, F.; Deng, Y. Low-temperature CO oxidation over supported Pt, Pd catalysts: Particular role of FeO_x support for oxygen supply during reactions. *J. Catal.* **2010**, *274*, 1–10. [CrossRef]
20. Deng, H.; Li, X.; Peng, Q.; Wang, X.; Chen, J.; Li, Y. Monodisperse magnetic single-crystal ferrite microspheres. *Angew. Chem. Int. Ed.* **2005**, *44*, 2782–2845. [CrossRef] [PubMed]
21. Choi, K.-H.; Chae, W.-S.; Kim, E.-M.; Jun, J.-H.; Jung, J.-H.; Kim, Y.-R.; Jung, J.-S. A Facile Fabrication of FeO/ZnO Core-Shell Submicron Particles with Controlled Size. *IEEE Trans. Mag.* **2011**, *47*, 3369–3372. [CrossRef]
22. Mustafa, M.D.; Mehmet, A.G.; Yusuf, Z.M. Palladium Nanoparticles by Electrospinning from Poly(acrylonitrile-*co*-acrylic acid)−$PdCl_2$ Solutions. Relations between Preparation Conditions, Particle Size, and Catalytic Activity. *Macromolecules* **2004**, *37*, 1787–1792.
23. Tongjie, Y.; Tieyu, C.; Xue, F.; Fang, C.; Jie, W. Preparation of yolk–shell Fe_xO_y/Pd@ mesoporous SiO_2 composites with high stability and their application in catalytic reduction of 4-nitrophenol. *Nanoscale* **2013**, *5*, 5896–5904.
24. Yoo, S.-G.; Kim, J.-H.; Kim, U.-H.; Jung, J.-S.; Lee, S.-H. Comparison of the Kinetic Behaviors of Fe_2O_3 Spherical Submicron Clusters and Fe_2O_3 Fine Powder Catalysts for CO Oxidation. *Bull. Korean Chem. Soc.* **2014**, *35*, 1379–1384. [CrossRef]